

Muon Catalyzed Fusion in 3 K Solid Deuterium.

P.E. Knowles*, G.A. Beer, G.R. Mason, T.A. Porcelli
University of Victoria, Victoria B.C., Canada, V8W 2Y2

A. Adamczak
Institute of Nuclear Physics, Cracow, Poland

J.M. Bailey
Chester Technology, England

J.L. Beveridge, G.M. Marshall and A Olin
TRIUMF, 4004 Wesbrook Mall, Vancouver B.C., Canada, V6T 2A3

M.C. Fujiwara
University of British Columbia, Vancouver B.C., Canada, V6T 2A6

T.M. Huber
Gustavus Adolphus College, St. Peter, Minnesota 56082

R. Jacot-Guillarmod, and F. Mulhauser
Institut de Physique, Université de Fribourg, CH-1700 Fribourg, Switzerland

P. Kammel[†], and J. Zmeskal
Austrian Academy of Sciences, A-1090 Vienna, Austria

S.K. Kim
Jeonbuk National University, Jeonju City 560-756, South Korea

A.R. Kunselman
University of Wyoming, Laramie, Wyoming 82071

C.J. Martoff
Temple University, Philadelphia, Pennsylvania 19122

C. Petitjean
Paul Scherrer Institut, PSI, CH-5232 Villigen, Switzerland

Muon catalyzed fusion in deuterium has traditionally been studied in gaseous and liquid targets. The TRIUMF solid-hydrogen-layer target system has been used to study the fusion reaction rates in the solid phase of D₂ at a target temperature of 3 K. Products of two distinct branches of the reaction were observed; neutrons by a liquid organic scintillator, and protons by a silicon detector located inside the target system. The effective molecular formation rate from the upper hyperfine state of μd and the hyperfine transition rate have been measured: $\tilde{\lambda}_{\frac{3}{2}} = 2.71(7)_{stat.}(32)_{syst.} \mu s^{-1}$, and $\tilde{\lambda}_{\frac{3}{2}\frac{1}{2}} = 34.2(8)_{stat.}(1)_{syst.} \mu s^{-1}$.

*Present Address: Institut de Physique Nucléaire, Université Catholique de Louvain, B-1348, Louvain-La-Neuve, Belgium.

[†]Present Address: University of California, LBNL, Berkeley, California 94720

The molecular formation rate is consistent with other recent measurements, but not with the theory for isolated molecules. The discrepancy may be due to incomplete thermalization, an effect which was investigated by Monte Carlo calculations. Information on branching ratio parameters for the s and p wave $d + d$ nuclear interaction has been extracted.

I. INTRODUCTION

For forty years it has been known that the introduction of a negative muon into a mixture of the three isotopes of hydrogen (protium, deuterium, and tritium) can lead to fusion reactions between the hydrogen nuclei, a process called muon catalyzed fusion or μCF . The intricately connected molecular, atomic, and nuclear processes that occur have taken many years to identify and offer a richness of physics in both theoretical and experimental domains [1–4].

The TRIUMF solid-hydrogen-layer target system [5] was used to measure μCF in solid deuterium for the first time. The preliminary results [6,7] from our experiment at low temperature were in sharp disagreement with theory and initiated further investigations of the reactions in solid D_2 [8–11]. This work presents our final results based on larger statistics and the simultaneous observation of two distinct branches of the fusion reaction.

The μCF reaction in pure deuterium has been well investigated for gaseous and liquid targets—see Refs. [12,13] and references therein—where the assumption that the D_2 is not interacting with its neighbors has been used in the theoretical analysis. That approximation has led to generally good agreement between theory and experiment when the deuterium is a fluid. The data presented here from μCF in solid deuterium maintained at 3 K indicate that it fails.

II. THEORY

A. Physical Processes

A negative muon introduced into pure deuterium slows and captures on a deuteron to form an excited μd in a characteristic time of picoseconds in high density targets such as solids or liquids [14–16]. The subsequent deexcitation of the muonic atom occurs via Stark, Auger, scattering, radiative, and transfer processes, which occur on the 100 ps time scale [17]. The process $(\mu d)_{n_i} + d \rightarrow (\mu d)_{n_f} + d$ with $n_f < n_i$, often called Coulomb deexcitation, provides a source of acceleration for the muonic atom since the final state contains only the massive particles which share the energy released in the $n_i \rightarrow n_f$ transition. The subsequent energy distribution of the μd contains both thermal and epithermal (nonthermalized) components of muonic atoms. The relative populations reflect the temperature and density of the muonic atoms' environment [18–21].

Once the atomic ground state has been reached, the reactions of the μd are dominated by the scattering from D_2 molecules, including inelastic processes such as the realignment of the μd hyperfine state, or the formation of the molecular bound state $d\mu d$.

A muonic deuterium atom may form a molecule or molecular ion via two mechanisms. The first is the capture of the muonic atom on one nucleus of a deuterium molecule to form a molecular bound state with the subsequent release of the bound state energy by an Auger process:



A second process, a resonance mechanism first proposed by Vesman [22], is a curiously fortuitous effect that depends on the energy levels of all the involved bound states. The existence of a state of the $(d\mu d)$ bound by ~ 2 eV allows the excess energy of the system, the energy liberated in molecular formation plus the incident μd energy, to be absorbed in the excitation of rotational and vibrational

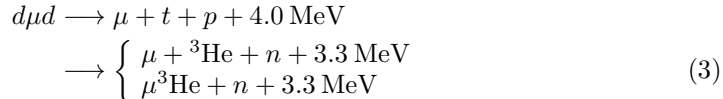
states, $(\nu_f K_f)$, of the full six body final state (strongly bound states liberate energy above the dissociation threshold of the D_2). A resonance in the formation cross section occurs when the incident energy of the μd_F in hyperfine state F is such that the total initial energy of the system matches the energy of some set of final state excitation parameters,

$$\mu d_F + [ddee]_{\nu_i, K_i} \rightarrow [(d\mu d)_{J\nu} dee]_{\nu_f, K_f}. \quad (2)$$

Here, J and ν refer to the orbital angular momentum and vibrational quantum number respectively, while the $\nu_{i,f}$, and $K_{i,f}$ refer to the vibrational quantum number and rotational quantum number of the six-body system. The resonant formation process has been well studied, resulting in calculations of the energy dependence of the rate [23–27].

Calculation of an effective formation rate which can be compared to experiment must assume an energy distribution of the μd atoms in the D_2 target. The distribution, which is determined by the initial energy at which the μd was formed and the subsequent energy loss processes, is convoluted with the reaction rates at an appropriate temperature to produce an overall temperature dependent rate [12]. The agreement between theory, which predicts a rapid thermalization of the μd and hence uses a μd population in thermal equilibrium with the surrounding deuterium, and experiments which use liquid and gas targets, is good (see Fig. 1). The results of present measurements in solids are in disagreement.

The small size characteristic of the muonic molecular bound states is such that nuclear fusion can occur. For deuterium, there are two fusion channels:



Once fusion occurs, the muon is generally set free and can begin the process again (cycling); however, the $Z = 2$ helium nucleus can sometimes capture the muon into atomic orbital bound states stopping further reactions, a process called sticking. The number of fusion cycles in which the muon participates is limited by the muon lifetime and by the sticking probability. The kinetics for the cycle shown in Fig. 3 are given in the Appendix.

The energy difference between the two hyperfine states of the μd is 48.5 meV; the energy is readily liberated in processes which depopulate the upper spin state. There is a disagreement between theory and experiment for the hyperfine transition rate $\bar{\lambda}_{\frac{3}{2}, \frac{1}{2}}$, a situation which is well discussed in Scrinzi *et al.* [12]. As indicated in Fig. 2, theory models the shape of the temperature dependence, but the calculated rate is too high. Given the agreement between the calculated and measured formation rates (Fig. 1) and the accuracy in the calculations for the scattering reactions (which are expected to be correct to 10%), the discrepancy is not understood.

B. Monte Carlo Studies

The two-node approximation (Appendix) assumes that the rates used to represent the various processes are time independent, or, equivalently, the result after convoluting the μd energy distribution with the energy dependence of the rates remains constant in time. Since the calculations of the muonic processes give energy dependent rates, it is natural to use the Monte Carlo method to study the time evolution of the muonic atom energy distribution and thus the interplay between all the energy dependent rates.

Until recently, only scattering cross sections for muonic atoms on free hydrogen isotopes were available. Monte Carlo simulations predicted that the time required to thermalize a muonic atom after formation was very short (20 ± 20 ns in D_2 gas at 5% of liquid density, shorter times at higher density). After rapid thermalization, the energy distribution of the atoms was constant in time making the formation rates time independent and thus validating the two-node approximation.

At low energies, μd elastic scattering on a solid lattice does not reduce the μd lab kinetic energy due to the large mass of the recoiling crystal. It was initially suggested by M. Leon that mechanisms for energy loss might be curtailed for muonic atoms in solid hydrogen isotopes. First quantitative calculations of the energy dependent scattering cross sections in solids have been completed [28]. In Fig. 4 the scattering cross section for $F = \frac{3}{2} \mu d$ atoms on a solid ortho-deuterium target at 3 K and zero pressure is shown. The total cross section includes elastic scattering on the *fcc* lattice of frozen D_2 molecules and inelastic scattering processes—phonon transitions and rovibrational excitations of the D_2 molecules. The μd deceleration rate is determined by the inelastic processes because of the large recoil mass in elastic scattering processes. The rovibrational excitation threshold is about 10 meV, and below that the μd atoms lose energy in purely phonon scattering, an amplitude which also falls rapidly with decreasing μd energy. In Fig. 4 the inelastic cross section for μd in solid D_2 is compared to the doubled nuclear $\mu d + d$ cross section which represents the first-order approximation to the free molecular D_2 cross section [29,30].

Based on the new rate calculations, a Monte Carlo simulation predicting the time spectra of fusion products from an infinite solid D_2 lattice has been performed. The resulting spectra were fit with the same kinetics function as the real data to extract effective rates. The analysis of the Monte Carlo spectra will be presented after discussing fits to the data.

The suppression of the inelastic scattering probability in solid deuterium implies a slow thermalization rate for any epithermal μd atoms, which in turn means that the energy distribution of the muonic atoms can *not* be assumed to be constant in time. The implications of these effects on the use of the two-node approximation are given in the discussion section.

III. EXPERIMENTAL EQUIPMENT

A description of the cryogenic target system used in this measurement has been presented elsewhere [5,31]. In brief, a continuous-flow liquid helium cryostat was used to cool two 51 μm thick gold foils to 3 K (Fig. 5). A gas spraying system directed the deuterium toward the adjacent surfaces of the foils where it condensed and froze, creating a solid deuterium film maintained in a high vacuum. A palladium filter, which operated above 600 K, was used to purify the D_2 immediately prior to freezing so the ratio of even to odd molecular spins was expected to be statistical (nD_2) [32]. Muons entered the deuterium after passing through one thin gold foil, which acted as a degrader, and stopped either in the first or second solid hydrogen layer, or in the gold itself. Muon catalyzed fusion of $d\mu d$ molecules then occurred. The higher energy fusion products, neutrons at 2.45 MeV and protons at 3.02 MeV, were detected.

Measurements with solid layers of D_2 and 1H_2 were made. Two different layer thicknesses of solid deuterium, 10.54(53) $\text{mg} \cdot \text{cm}^{-2}$ (herein called thick) and 2.11(11) $\text{mg} \cdot \text{cm}^{-2}$ (thin), $\sim 40 \text{ cm}^2$ in area, were frozen onto the foils [33]. The thick D_2 layer received an integrated muon flux of $220 \times 10^6 \mu$ with 53(3)% stopped in the solid layer, while the thin layer received $164 \times 10^6 \mu$ with a stopping fraction

of 14(2)%. The study of the background in ${}^1\text{H}_2$ (where there is no strong fusion process) for both thicknesses above and for bare target conditions was done with $130 \times 10^6 \mu$. Table I summarizes the data.

A. The Trigger

The timing diagram for the trigger electronics is shown in Fig. 6. When the T1 scintillator (see Fig. 5) signaled the entrance of a muon, two gates were opened: B to indicate that a muon was in the target, and EVG, the event gate. If any of the detectors recorded an event at a time when EVG was true, such as the pictured TPn, the corresponding TRGn gate was opened. At the end of the event gate duration, the logical OR of all possible TRGn gates was placed in coincidence with the end of the event gate, EEVG, to determine whether the event was read (an event trigger) or cleared. Events for which a second muon arrived in the target within $\pm 10 \mu\text{s}$ were discarded either by inhibiting the trigger or during analysis based on an event flag. An event trigger immediately initiated a hardware inhibit to prevent loss of the data already measured. A computer-driven signal maintained the inhibit while the data were read and while the CAMAC modules were cleared. An event clear would inhibit the trigger system and then remove any values accidentally recorded by the CAMAC system.

B. Neutron Detectors

The arrangement of detectors is shown in Fig. 5. Each neutron detector was a 12.5 cm diameter by 10 cm deep cylinder of NE-213 liquid scintillator viewed by a photomultiplier. Hardware-based pulse shape discrimination was used to differentiate between photon and neutron events. Uncharged particles were selected by an anticoincidence with both members of a pair of charged-particle scintillators [EiN1 and EiN2 for ($i = 1, 2$) in Fig. 5]. Since photon events were very common, prescaling was done to keep the photon triggers to an acceptable level. Typical neutron rates during the measurements were less than 150 s^{-1} .

An effective method for background suppression in μCF processes is the requirement that the muon survive the event, a condition enforced by the detection of the muon decay electron. This delayed electron, or *deLe*, condition was satisfied if the muon decay electron was detected between 0.2 and $5.05 \mu\text{s}$ after the time of a candidate fusion event. It strongly enhanced the signal-to-background ratio of the data. Electrons from muon decay were detected by the coincidence of either pair of charge-veto scintillators.

The time spectrum of the decay electrons was used to determine the proportion of muons stopped in hydrogen. Decay electrons were generated either with a free muon lifetime ($2.2 \mu\text{s}$), or the lifetime of muons in Au (79 ns). The intensity of each lifetime component was proportional to the number of muons stopped in the respective material.

C. Silicon Charged-Particle Detectors

A fully depleted, ion implanted silicon detector of 600 mm^2 active area was mounted inside the vacuum system to detect the charged fusion products. Its $150 \mu\text{m}$ active thickness was sufficient to measure protons of up to 4 MeV, and

was well suited for detecting the fusion protons at (or below) 3.02 MeV. The detector was mounted on the cryostat cold shield, in front of the neutron detector N1, and viewed the solid deuterium layers directly (see Fig. 5). At the nominal operating voltage of 30 V the best energy resolution achieved was 170 keV FWHM due to mounting constraints and the resulting long cable to the preamplifier. The 3 MeV protons produced by dd fusion were easily seen but the tritons and ^3He were too low in energy and hence obscured in background or stopped in the solid target before reaching the detector. The rate from silicon detector events was about 25 s^{-1} .

IV. ANALYSIS

A. Neutron Spectra

Three main event types occur in the neutron spectrum: fusion neutrons, capture neutrons, and neutrons from the ambient background (zone neutrons). Fusion neutrons, which constitute the signal, are generated with a time distribution n_f , according to the kinetics of the muon catalyzed fusion reactions in the target and are thus time correlated with the muon arrival and will satisfy the del_e condition with the efficiency ϵ_e with which the electron detectors measure that a muon has decayed in the delayed time interval 0.2–5.05 μs . This efficiency is comprised from a solid angle contribution and the time window efficiency:

$$\epsilon_e = \Omega_e \lambda_o \int_{0.2\ \mu\text{s}}^{5.05\ \mu\text{s}} d\tau e^{-\lambda_o \tau}. \quad (4)$$

Neutrons from nuclear muon capture, with time distribution n_c , are also time correlated with the arrival of the muon according to the capture and decay lifetimes, but are obviously not followed by a muon decay electron. Only those capture neutrons that are followed by some accidental event in the electron detectors will be admitted to the del_e spectrum (with efficiency ϵ_a).

The neutron events from the ambient flux contribute a constant background, n_z . These events pass the del_e cut depending on the time t of the neutron with respect to the muon arrival t_0 . The del_e condition requires an event in the electron detectors between 0.2 μs to 5.05 μs after the neutron. For a neutron that occurs more than 5.05 μs before the muon arrival, only an accidental del_e condition with efficiency ϵ_a can pass the event into the del_e spectrum. As the time of the ambient background neutron event moves closer to the subsequent arrival of the muon, more of the cut interval overlaps with the time when a muon is known to be in the target and hence the efficiency for accepting the neutron grows. For a neutron event occurring 0.2 μs before the muon arrival, the time selection interval overlaps exactly with the muon arrival, hence the muon decay selects the background event with an efficiency slightly larger than the decay electron efficiency ϵ_e . After the muon arrival, accidental events are accepted with the electron detection solid angle efficiency weighted by the exponential probability that a muon had survived to the time of neutron detection. The flat background, n_z , thus acquires a muon lifetime dependence in the delayed spectrum. This relationship is represented by the integral term in Eq. (6). The efficiency ϵ_a appears in all terms since an accidental del_e condition permits neutrons into the del_e spectrum regardless of the neutron source.

The raw (without the del_e condition) and del_e spectra are given by:

$$n_r = n_f + n_c + n_z \quad (5)$$

and

$$n_{del_e} = (\epsilon_e + \epsilon_a) n_f + \epsilon_a n_c + \left(\epsilon_a + \Omega_e \lambda_o \int_{t+0.2 \mu s}^{t+5.05 \mu s} d\tau \Theta(\tau - t_0) e^{-\lambda_o(\tau - t_0)} \right) n_z, \quad (6)$$

where $\Theta(\tau - t_0)$ is a step function which models the discrete arrival time of the muon.

Combining (5) and (6) gives:

$$n_{del_e} = \epsilon_e n_f + \epsilon_a n_r + \left(\Omega_e \lambda_o \int_{t+0.2 \mu s}^{t+5.05 \mu s} d\tau \Theta(\tau - t_0) e^{-\lambda_o(\tau - t_0)} \right) n_z. \quad (7)$$

Note that knowledge of the unknown capture time spectrum, n_c , is not required. The largest contribution to the background is from the accidental *del_e* coincidences, and is proportional to the raw distribution n_r , a spectrum well measured during the experiment and having small uncertainties. The events in the *del_e* spectrum occurring in the short time interval measured before the muon arrival determine the value of n_z .

In Eq. (7) there are two input spectra, each with an uncertainty. Replacing the integral by the symbol $I(t)$, we have

$$n_{del_e} \pm \delta n_{del_e} = \epsilon_e n_f + \epsilon_a (n_r \pm \delta n_r) + I(t) n_z. \quad (8)$$

The efficiency factor ϵ_e will eventually be absorbed in a fitted normalization constant, so it does not need to be determined independently.

The weights for the χ^2 fit depend on the input spectra uncertainties;

$$\text{weight} = \left[(\delta n_{del_e})^2 + (\epsilon_a \delta n_r)^2 \right]^{-1}. \quad (9)$$

The weights contain the variable ϵ_a , so the fitting routine was iterated, each time re-evaluating the weights, until a stable value for ϵ_a was found. Figure 7 shows the data and the fitted curve.

B. Proton Spectra

The proton spectra exhibited many features, and careful study of five different types of target was necessary to extract meaningful parameters. The different target conditions were: bare target, thick and thin solid *protium* layers upstream and downstream, and thick and thin solid *deuterium* layers upstream and downstream (see Table I).

1. Energy Spectra

The fusion protons are produced at 3.02 MeV, but lose energy in the target resulting in a broad distribution: Fig. 8 shows the spectrum taken with the thick deuterium target. The background comprises about 20% of the total counts.

The background in the detector comes mainly from charged particle emission following nuclear muon capture. Protons are the most commonly emitted particle with a spectrum which is suppressed for energies below the nuclear Coulomb barrier. The emission probability ranges from 15% for muon capture on silicon—with a

5 MeV Coulomb barrier—down to about 1% following muon capture on gold where the Coulomb barrier is about 16 MeV [34]. The relative intensity of the background depends on the thickness of the hydrogen layers and the incident muon momentum which together determine the ratio of muons stopped in the gold target support foil or detector silicon to those stopped in the hydrogen target itself. Thick hydrogen targets exhibited less background.

The background in the silicon detector was removed to the ϵ_a level by the *deLe* requirement, evidence that the background was due to a process which consumed the muon. The ϵ_a measured by the ratio of the number of counts above the 3 MeV fusion limit (hence nonfusion related), to those from the same spectrum after applying the *deLe* cut gave a value of 0.11(4)%, which is in agreement with the value found for ϵ_a from the neutron detector: 0.14(4)%.

2. Time Spectra

Time spectra for each of the five target types were collected for 23 different energy windows, each 142 keV wide (the intrinsic energy resolution was 170 keV), beginning at 0.9 MeV. They were examined for number, intensity, and value of visible lifetimes, and time-zero value. For data where fusion events contributed to the spectrum the characteristic two-lifetime form of the kinetics in pure deuterium allowed an accurate measure of t_0 for that energy window, as well as the intrinsic time resolution of the detector at that energy.

The silicon detector exhibited time walk. Thick deuterium data (see Table I) were chosen to measure the energy dependent correction since the fusion protons provided a well defined time zero, and the energy loss in the layer distributed the signal over the energy range 1–3 MeV. Walk gave a 30 ns correction between the 3 MeV and the 1 MeV time spectra, where the difference in proton flight times at the different energies was no more than 4 ns.

Two standard energy regions were defined from which the time spectra were selected for further analysis. The lower energy signal region, called *l*, was limited to 2.3–2.7 MeV; below 2.3 MeV the time resolution was poor enough that it began to obscure the structure of the fast lifetime component in the fusion signal. The limit at 2.7 MeV was selected to favor fusions occurring away from the surface of the layer, where the possibility of μd escape from the layer would not affect the kinetics representation. The higher energy background region, called *h*, was selected between 3.3–4.0 MeV, where there were no fusion events. Walk-corrected data were then selected for the *h* and *l* regions.

Figure 9 shows the time spectra for the *h* and *l* energy cut regions for the thick deuterium, bare target, and thick protium runs. Two lifetimes are the dominating feature in the thick deuterium data, (A), as expected from the two-node approximation. The fusion spectrum has a rapid onset and rise of the leading edge, a shape given by the time resolution of the detector and not by the physical processes of muon stopping, atomic capture, and thermalization.

The spectra without fusion signals, the *h* and *l* regions for both gold and thick protium and the *h* region for thick deuterium, seem delayed with respect to the fusion signal. It is possible to extract two lifetimes from the background spectra as well—lifetimes consistent with muons in gold (80 ns) and muons in intermediate mass nuclei like silicon or aluminum (~ 700 ns). The background does not pass the *deLe* requirement except by ϵ_a coincidence, however the fusion statistics in the *deLe* spectrum were insufficient for the kinetics analysis.

The background in the fusion spectrum was parametrized and removed phenomenologically. Studies of the *h* and *l* time spectra for targets that did not produce

fusion signals provided the method to predict the background in the l region given the spectrum in the h region. Scaling from the h region to the l region was time dependent, *i.e.*,

$$l(t) = f(t) \times h(t). \quad (10)$$

This is consistent with a background of charged particles emitted after muon capture on differing nuclei. Each capture spectrum contributes to the overall time spectrum with an intensity dependent on the chosen energy range. Since the energy spectra of the emissions are nuclei dependent, the overall time spectrum cannot be expected to be independent of energy. The function $f(t) \pm \delta f$, parametrized in four variables A_i via

$$f(t) = \left[A_1 + A_2 e^{-A_3(t-A_4)} \left(1 - e^{-A_3(t-A_4)} \right) \right], \quad (11)$$

was found using Eq. (10) to fit the h and l time spectra from both thin and thick protium layers; δf was found from the covariance matrix of the A_i .

Since the *deLe* condition was not imposed on the fit data, the l spectra containing fusion signals were simply composed of the fusion protons and the background. The fit expression, with uncertainties, was

$$p_l \pm \delta p_l = p_f + (f \pm \delta f)(p_h \pm \delta p_h) \quad (12)$$

where p_l was the measured time spectrum in the l energy window, p_h was from the h energy window, p_f was the kinetics function, after convolution with the detector resolution, for proton production by μ CF, and f was the background transformation function as above.

The weight for each fitted point was constructed in the same manner as in the neutron case, yielding:

$$\text{weight} = \left[(\delta p_l)^2 + (f \delta p_h)^2 + (p_h \delta f)^2 \right]^{-1}. \quad (13)$$

C. Fit Methods

The data were fit with a function made by convoluting the theoretically expected time distributions, Eq. (19) of the Appendix, with a Gaussian detector time resolution and a step function modeling the muon arrival. The time spectra data were rebinned with an adaptive step size which preserved the fine binning where sensitivity to fast rates was required, but used larger steps at long times where small scale sensitivity was not needed. The larger bins at long times eliminated the problem of fitting data containing many zeros, and reduced the total number of points in the fit, which in turn significantly reduced the amount of computer time required per fit.

Excluding background parametrization, six independent parameters were required to completely determine the shape of a spectrum: two lifetimes, two amplitudes, the detector timing resolution σ , and the muon arrival time t_0 . There are ten kinetic parameters which determine the values of the lifetimes and amplitudes, and so it is impossible to measure more than four of them at any one time. Since an absolute measurement was not done, one of the parameters was used for normalization, so only three of the ten kinetics parameters could be extracted from a single time spectrum. By fitting both neutron and proton data simultaneously, four kinetics parameters could be extracted (equivalent to an absolute measurement for

a single fusion product spectrum). The parametrization of the background in the data introduced other parameters which were independent of the kinetics. The fit to the data was made by χ^2 minimization.

The fits to the spectra were sensitive to the values of $\tilde{\lambda}_{\frac{3}{2}\frac{1}{2}}$, $\tilde{\lambda}_{\frac{3}{2}}$, $\phi_z\lambda_z$ (the loss rate to target contaminants heavier than hydrogen, predominantly nitrogen), $\tilde{\lambda}_{\frac{1}{2}}$, P_s , β_s , and β_p (see Fig. 3 and the Appendix for the definition of the parameters). The standard values of the parameters passed to the fitting routine are given in Table II, along with the uncertainty on the value used when examining the systematic uncertainties.

D. Fit Results

For both neutron and proton data, fits were made to the individual time spectra. Neutron data were restricted to the thick deuterium targets only, since insufficient statistics existed for the thin deuterium layers. For the proton data, both thick and thin deuterium layers yielded spectra which could be fit.

In the fits to individual spectra, the two kinetics parameters $\tilde{\lambda}_{\frac{3}{2}\frac{1}{2}}$ and $\tilde{\lambda}_{\frac{3}{2}}$, as well as the loss rate to high-Z components, $\phi_z\lambda_z$, were measured. When the fits to the combined spectra were done, the sensitivity to four parameters was used to measure $\tilde{\lambda}_{\frac{3}{2}\frac{1}{2}}$, $\tilde{\lambda}_{\frac{3}{2}}$, $\phi_z\lambda_z$, and values for $\tilde{\lambda}_{\frac{1}{2}}$, P_s , β_s , and β_p , each taken in turn with the remaining three of the four fixed at the standard values (see Table II).

1. Uncertainties

The systematic uncertainties fall into two categories; the effects on the measured values resulting from uncertainties in input parameters, and the effects due to variations in the fit interval, cuts on the input spectrum, and, in the case of the proton spectrum, the background scaling function. The uncertainties due to input parameters in the fit are relatively easy to identify and to understand by changing the parameter and refitting the data. The systematic effects due to the cuts on the spectrum and the fitting interval were studied by fitting the same data with different cuts. The fit was considered satisfactory when the variations on the fit parameters with cut value were small with respect to the other systematic and statistical uncertainties.

Within the stated uncertainty, the values found for the fitted parameters were not affected by variations in temperature T (used to make $\tilde{\lambda}_{\frac{1}{2}\frac{3}{2}}$ from the $\tilde{\lambda}_{\frac{3}{2}\frac{1}{2}}$ rate via detailed balance), density ϕ , muon decay rate λ_o , the detection efficiency ϵ (which was detector dependent), and ω_s . This was checked by changing the input values of the above parameters by twice their respective uncertainties and confirming no variation in the fitted parameters. The uncertainty in the input values of $\tilde{\lambda}_{\frac{1}{2}}$, β_s , β_p , and P_s did have significant systematic effects.

The total systematic uncertainty on a fitted parameter was determined by the addition in quadrature of the uncertainties due to the possible variations of the fixed input parameters. The systematic uncertainty associated with the proton background scaling function was handled in a different way. The uncertainty in the background scaling function was explicitly taken into account in the fitting function, and so the uncertainty due to the scaling is included in the statistical error evaluation (see §IV D 3 below). Asymmetric uncertainties were determined by the change necessary to increase the χ^2 of the fit by 1.0, however, in no case were the uncertainties strongly asymmetric.

2. Neutron Data Fits

Fits to the thick deuterium neutron data are summarized in Table III and plotted in Fig. 7. The fitted value for the ϵ_a efficiency agrees with values measured from neutrons above the fusion energy edge, measurements with the protium targets, and with measurements made with the silicon detector. The σ value for the time resolution of the detector yields a FWHM of 3.5 ns, in accord with the flight time of 2.45 MeV neutrons traversing a 10 cm deep detector.

3. Proton Data Fits

Fits to the proton data taken from both the thick and thin deuterium layers are summarized in Table III; the results of the fit for the thick target data are plotted in Fig. 10. The results for the thick deuterium given in the table are in reasonable agreement with the neutron results in Table III. The signal-to-background ratio for the thick deuterium proton data was roughly 9:2, while the ratio for the thin deuterium data was three times worse at 9:6. The background scaling function was predicted using both the thick and thin protium layers and so, to check the systematic effects on the fits, the two deuterium spectra were each fitted with both of the scaling functions. The results of the fits showed that the thick deuterium data were not sensitive to the choice of background scaling, presumably due to the favorable signal-to-background ratio, while the thin deuterium fits fluctuated to the limits of the statistical accuracy. The data extracted from the thin deuterium targets were more sensitive to other effects such as μd escape from the layer and, from the value of $\phi_z \lambda_z$, suffered from a higher contamination.

4. Simultaneous Fits to Both n and p Spectra

The simultaneous fit of both the neutron and proton data from the thick deuterium target allowed one more kinetic parameter to be measured. The choice was limited to $\lambda_{\frac{1}{2}}$, β_s , β_p , and P_s : the kinetics equations were not sufficiently sensitive to other parameters. All of the fits gave a χ^2 value of 325 for 309 degrees of freedom.

With $\lambda_{\frac{1}{2}}$ and any two of P_s , β_s , and β_p fixed, a value for the remaining parameter was found. The results of the fit, which yielded values for P_s , β_s , and β_p , in addition to $\tilde{\lambda}_{\frac{3}{2}\frac{1}{2}}$, $\tilde{\lambda}_{\frac{3}{2}}$, and $\phi_z \lambda_z$, are given in columns 2–4 of Table IV.

The values of $\tilde{\lambda}_{\frac{3}{2}\frac{1}{2}}$, $\tilde{\lambda}_{\frac{3}{2}}$, and $\phi_z \lambda_z$ do not change during the fits to P_s , β_s , and β_p , behavior which is expected from Eq. (16) which enters the kinetics as a distinct subformula. The large systematic uncertainty in the $\tilde{\lambda}_{\frac{3}{2}}$ value is due almost entirely to the uncertainty in the $\tilde{\lambda}_{\frac{1}{2}}$ input value.

Fixing P_s , β_s , β_p at the standard values allowed a measurement of $\tilde{\lambda}_{\frac{1}{2}}$, presented in the last column of Table IV. For this fit, systematic uncertainty in the parameters is dominated by the uncertainty in the β_p input value.

E. Fits to the Monte Carlo Simulations

A Monte Carlo (MC) simulation has been performed using the calculated (Ref. [28]) energy-dependent rates for μd atom scattering on solid deuterium at 3 K, calculated rates of $d\mu d$ molecule formation (resonant and nonresonant) on

a free D_2 molecule and back-decay rates of the $(d\mu d)d$ complex [25,27]. Since the solid target used was a statistical mixture of ortho- and para-deuterium (nD_2), the μd scattering on D_2 molecules in both $K = 0$ and $K = 1$ initial rotational states has been taken into account. The muon transfer from μd atoms to high- Z contamination has been described by a constant muon transfer rate.

Recent experiments [21,35] and theory [19] show that the initial distribution of μd energy contains an admixture of nonthermalized (in the region of 1–10 eV) μd atoms. The initial μd energy in our MC has been described by a sum of two Maxwell distributions. One of them, corresponding to atoms thermalized at 3 K, has a mean energy of 0.4 meV. The hot μd atoms are assumed to have a mean energy of 1 eV. The details of the shape of the high-energy component are not important for this simulation because the deceleration rate at energies greater than about 0.1 eV is very high. Therefore, the main input parameter to the Monte Carlo is the relative intensity of the energetic μd population. The second important parameter is a scaling factor for the energy-dependent nonresonant spin flip rate $\lambda_{\frac{3}{2}\frac{1}{2}}(E)$, to account for the disagreement between theoretical results and experiment (see [12]).

A qualitative agreement with the two-node kinetics model has been reached by a proper choice of the two important parameters of the Monte Carlo. Fitted MC spectra yield values of $\tilde{\lambda}_{\frac{3}{2}}$ and $\tilde{\lambda}_{\frac{3}{2}\frac{1}{2}}$ consistent with experiment if the scaling factor for the theoretical nonresonant spin flip rate is about 0.5 and the relative population of the hot μd 's is near 0.75. However, this fit of the kinetics function to the early-time part of the neutron and proton MC spectra does not yield satisfactory values of χ^2 . This result is probably due in part to the lack of a correct form of the energy-dependent $d\mu d$ resonant molecular formation rate below about 10 meV, in solid deuterium at 3 K and zero pressure.

Figure 11 shows the experimental neutron data in comparison to the output of the MC simulation. The spectrum at long times, when μd atoms disappear mainly via nonresonant $d\mu d$ formation and muon transition to the $Z > 1$ contaminants, is well described by the MC simulations and good values of χ^2 are obtained ($\chi^2 = 33.5/30$ points). This is so since the rates for nonresonant $d\mu d$ formation, in both the $J = 0$ and $J = 1$ states, are not strongly energy dependent below 10 meV, meaning that the detailed shape of the μd energy distribution is not significant. The disagreement at times dominated by the quartet to doublet hyperfine transition and thermalization is clearly visible as the steeper slope in the MC spectrum.

V. DISCUSSION AND CONCLUSIONS

Results derived from our experiment show that the processes governing molecular formation in the solid state are not yet quantitatively understood, but qualitative consistency has been achieved with the theory of slow thermalization caused by solid state effects [28].

1. Kinetics Parameters

The values presented in Table IV for the kinetics parameters (under the assumptions inherent in the two-node approximation) represent the first examination of the muon catalyzed fusion process in solid D_2 .

The qualitative success of the Monte Carlo simulation of fusion in solid D_2 is a clear indication that slow thermalization effects are important. It is surprising that the two-node approximation works at all in this situation. Why it does work can be seen by examining the processes themselves.

For $\mu d_{\frac{3}{2}}$, slow thermalization at the lowest energies allows molecular formation via the lowest resonances. Even so, spin deexcitation processes and thermalization remove μd from the resonant energy region at least ten times faster than the effective formation rate. Under such conditions, sensitivity to the shape of the resonance is suppressed and use of a constant rate is adequate.

Other explanations for the large $\tilde{\lambda}_{\frac{3}{2}}$ rate again rely on the solid state of the deuterium. Examination of Eq. (14) shows that an increase in $\tilde{\lambda}_f$, the deexcitation rate leading to fusion for the resonantly formed $[(d\mu d)_{J\nu}dee]$, will increase the effective formation rate by more successfully competing with the $\Gamma_{SF'}$ deexcitation (back decay). If there exists a sufficiently strong coupling of the rovibrational modes of the resonant six-body complex to phonons in the solid, then there may be sufficient augmentation of the deexcitation rate to increase $\tilde{\lambda}_f$. The molecular formation process occurring in solids has not yet been rigorously examined.

Since resonance formation involving $\mu d_{\frac{1}{2}}$ occurs at collision energies greater than 50 meV, the rapid initial cooling of the $\mu d_{\frac{1}{2}}$ permits only nonresonant molecular formation, thus assuming a time-independent nonresonant $\tilde{\lambda}_{\frac{1}{2}}$ rate is valid. Our measured value for $\tilde{\lambda}_{\frac{1}{2}}$ [= 0.052(8)_{stat.}(3)_{sys.} μs^{-1}] is in agreement with nonresonant molecular formation rates measured in other experiments [36]. However, the assumption that $\tilde{\lambda}_{\frac{1}{2}}$ measured in gas is appropriate for 3 K solid contributes the dominant systematic uncertainty in our measurement of $\tilde{\lambda}_{\frac{3}{2}}$.

The $\tilde{\lambda}_{\frac{3}{2}\frac{1}{2}}$ rate measures the disappearance rate for μd atoms capable of participating in resonant formation via $\tilde{\lambda}_{\frac{3}{2}}$ and thus contains hyperfine deexcitation from direct scattering, a contribution from back decay, *and* the effective rate of energy loss for the $\mu d_{\frac{3}{2}}$ which are in the energy window of the lowest resonance. Since our measured value for the effective hyperfine deexcitation is consistent with calculations of the rate due to scattering alone, the calculated rates are too large, a result consistent with recent μd + HD experiments [36].

Emission of the μd from the finite solid target layer is a loss mechanism that is not explicitly accounted for in the analysis, however the process would mimic the $\phi_z\lambda_z$ loss mechanism. We believe that the contamination was due to nitrogen, based on the observation of muonic nitrogen x rays. The value found for $\phi_z\lambda_z$, coupled with the value for the transfer to nitrogen, $\lambda_z \approx 10^5 \mu s^{-1}$, implies a nitrogen contamination of about 1.5 ppm, a value which was independently measured for the thick deuterium target via x-ray analysis. If the value were to represent only μd escaping from the layer, then roughly one third of all the μd atoms are emitted from the layer. Given the current understanding of the scattering cross sections, this process is unlikely to give such a strong effect. A Monte Carlo which includes the cross sections corrected for solid state effects as well as an accurate modeling of the finite geometry of the targets is required for the quantitative reinterpretation of the $\tilde{\lambda}_{\frac{3}{2}}$ and $\tilde{\lambda}_{\frac{3}{2}\frac{1}{2}}$ rates in terms of thermalization.

Demin *et al.* [11] have presented measured values for μCF rates in solid deuterium over a range of temperatures, assuming a similar kinetics function. Their results are consistent with ours, thus the disagreement with theory indicates that further calculations for the molecular formation rate in solid hydrogen must be made. The next experiments will have to examine the thermalization process, as well as the possible para-ortho effects. One suggested increase in the molecular formation rate for thermalized $\mu d_{\frac{3}{2}}$ occurs only for para-D₂ (*i.e.*, $J = 1$) [37]. Using a solid ortho-D₂ target would help to verify or discount that effect.

In solid hydrogen the molecular formation rate is concentration dependent, proportional to $c_d\phi N_o$, however, the thermalization rate is proportional to ϕN_o , since the scattering and energy loss processes for both $\mu d + D_2$ and $\mu d + {}^1H_2$ are similar for

low energy μd . If slow μd thermalization is the process increasing the $\tilde{\lambda}_{\frac{3}{2}}$ molecular formation rate, an experiment in a solid mixture of $D_2 + {}^1H_2$ using several values of the deuterium concentration will not yield the same reduced formation rate $\tilde{\lambda}_{\frac{3}{2}}$. Such an experiment in a $D_2 + {}^1H_2$ mixture would be more difficult to analyze, since the μp to μd transfer and subsequent creation of an epithermal μd would change the initial intensity of the epithermal μd atoms—the effect believed to be responsible for the elevated $\tilde{\lambda}_{\frac{3}{2}}$ rate.

2. Branching Ratios

Three values parametrize β_F , the effective branching ratio: β_s , β_p , and P_s , [cf. Eq. (16)]. Table IV lists fitted values for each of these parameters determined using standard values for the other two.

Our value $\beta_p = 0.563(14)_{stat.}(11)_{sys.}$ is close to the 0.59 predicted by theory (Hale, [38]), and is consistent with a previous measurement by Balin *et al.* [39]. Our value, $\beta_s = 0.487(15)_{stat.}(11)_{sys.}$, is consistent with 0.47, the prediction of Hale.

Standard values for β_s and β_p were used in a fit to P_s since β_s and β_p , as discussed above, were consistent with both theory and experiment. Faifman [25] predicts $P_s = 0.560$ at very low energy. Our result, $P_s = 0.47(8)_{stat.}(6)_{sys.}$ is in agreement. It should also be noted that the P_s value is dependent on the energy at which molecular formation occurs, so for μd atoms in the process of thermalizing, a constant P_s does not accurately represent the true physics processes.

ACKNOWLEDGMENTS

This work was supported by the Natural Sciences and Engineering Research Council (NSERC) of Canada, by a NATO Linkage Grant (LG 930162), and grants from DOE and NSF in the United States. A. Adamczak wishes to thank the Polish Committee for Scientific Research for support under Grant #2P03B01809. F. Mulhauser and R. Jacot-Guillarmod thank the Swiss National Science Foundation for support, and J.M. Bailey thanks the Leverhulme Trust.

APPENDIX: REACTION KINETICS

This appendix describes in more detail the kinetics equations derived from Fig. 3. All rates are normalized to liquid hydrogen density (4.25×10^{22} atoms \cdot cm $^{-3}$), and unit concentration, thus giving reduced rates for comparison with experiments under different conditions of concentration and density. The reduced rate of formation of $d\mu d$ molecules from a μd atom in the hyperfine state F is $\tilde{\lambda}_F$ [23]:

$$\tilde{\lambda}_F = \lambda_{nr} + \sum_S \lambda_{FS} \frac{\tilde{\lambda}_f}{\tilde{\lambda}_f + \sum_{F''} \Gamma_{SF''}}. \quad (14)$$

Molecular formation leading to fusion is composed of the nonresonant formation rate and the fraction of resonantly formed molecules which successfully fuse via $\tilde{\lambda}_f$ rather than resonantly scatter as characterized by $\Gamma_{SF'}$ [23]. Likewise, the reduced hyperfine transition rate from state F to F', $\tilde{\lambda}_{FF'}$, has contributions from regular scattering and from the decay of the resonantly formed $[(d\mu d)dee]$ complex:

$$\tilde{\lambda}_{FF'} = \lambda_{FF'} + \sum_S \lambda_{FS} \frac{\Gamma_{SF'}}{\tilde{\lambda}_F + \sum_{F''} \Gamma_{SF''}}. \quad (15)$$

Finally, β_F represents the fusion branching ratio for $d\mu d$ molecules formed from a μd in hyperfine state F. Experimentally, β_F is given by

$$\beta_F = \frac{\mu d_F + D_2 \rightarrow \mu + {}^3\text{He} + n}{(\mu d_F + D_2 \rightarrow \mu + p + t) + (\mu d_F + D_2 \rightarrow \mu + {}^3\text{He} + n)}.$$

The β_F measure will differ between the two hyperfine states due to the different distributions of bound state angular momenta selected by the hyperfine-dependent molecular formation processes [25]. The β_F parameters are convenient when writing the kinetics, but are composed of the more fundamental s and p wave fusion branching ratios, together with P_s , the ratio of s to p wave bound states from nonresonant formation [13]. Resonance formation always produces the p wave molecular state.

$$\beta_F = \frac{\lambda_{nr}}{\tilde{\lambda}_F} [P_s \beta_s + (1 - P_s) \beta_p] + \frac{\tilde{\lambda}_F - \lambda_{nr}}{\tilde{\lambda}_F} \beta_p. \quad (16)$$

The kinetics of the muon catalyzed reactions in pure deuterium are represented in Fig. 3. Using effective rates, the time evolution of the two different hyperfine populations can be approximated as a differential equation of the form:

$$\frac{d}{dt} \begin{pmatrix} N_{\frac{3}{2}} \\ N_{\frac{1}{2}} \end{pmatrix} = \begin{pmatrix} -A & B \\ C & -D \end{pmatrix} \cdot \begin{pmatrix} N_{\frac{3}{2}} \\ N_{\frac{1}{2}} \end{pmatrix} \quad (17)$$

with initial conditions η_F (normalized to a single muon)

$$\begin{pmatrix} N_{\frac{3}{2}}(t=0) \\ N_{\frac{1}{2}}(t=0) \end{pmatrix} = \begin{pmatrix} \eta_{\frac{3}{2}} \\ \eta_{\frac{1}{2}} \end{pmatrix} \quad \text{where} \quad \begin{cases} \eta_{\frac{3}{2}} = \frac{2}{3}, \\ \eta_{\frac{1}{2}} = \frac{1}{3}. \end{cases}$$

The coefficients in the matrix can be read from Fig. 3 giving (here all explicitly positive):

$$A = \lambda_o + \phi_z \lambda_z + \phi \left\{ \tilde{\lambda}_{\frac{3}{2}} \left[1 - \eta_{\frac{3}{2}} (1 - \epsilon) (1 - \omega_s \beta_{\frac{3}{2}}) \right] + \tilde{\lambda}_{\frac{3}{2} \frac{1}{2}} \right\}$$

$$B = \phi \left[\tilde{\lambda}_{\frac{1}{2}} \eta_{\frac{3}{2}} (1 - \epsilon) (1 - \omega_s \beta_{\frac{1}{2}}) + \tilde{\lambda}_{\frac{1}{2} \frac{3}{2}} \right]$$

$$C = \phi \left[\tilde{\lambda}_{\frac{3}{2}} \eta_{\frac{1}{2}} (1 - \epsilon) (1 - \omega_s \beta_{\frac{3}{2}}) + \tilde{\lambda}_{\frac{3}{2} \frac{1}{2}} \right]$$

$$D = \lambda_o + \phi_z \lambda_z + \phi \left\{ \tilde{\lambda}_{\frac{1}{2}} \left[1 - \eta_{\frac{1}{2}} (1 - \epsilon) (1 - \omega_s \beta_{\frac{1}{2}}) \right] + \tilde{\lambda}_{\frac{1}{2} \frac{3}{2}} \right\}.$$

The formal solution of Eq. (17) to obtain the time dependence of the hyperfine populations, $N_F(t)$, is tedious but straightforward. Once derived, the time structure of the fusion products, either protons or neutrons (generically denoted k), can be found by summing over the populations, formation rates, and branching ratios:

$$\frac{dk}{dt} = \phi \sum_{F=\frac{1}{2}, \frac{3}{2}} \alpha_F \tilde{\lambda}_F N_F \quad \text{with} \quad \alpha_F = \begin{cases} \beta_F & \text{for } k = n, \\ 1 - \beta_F & \text{for } k = p. \end{cases} \quad (18)$$

The time distribution of product k is thus:

$$\frac{dk}{dt} = \Psi_{\frac{3}{2}} e^{L_{\frac{3}{2}} t} + \Psi_{\frac{1}{2}} e^{L_{\frac{1}{2}} t}, \quad (19)$$

with rates which are the negatives of the the parameters:

$$L_{\frac{3}{2}} = \frac{-1}{2} \left[(A + D) + \sqrt{(A - D)^2 + 4BC} \right], \quad (20)$$

$$L_{\frac{1}{2}} = \frac{-1}{2} \left[(A + D) - \sqrt{(A - D)^2 + 4BC} \right], \quad (21)$$

and amplitudes:

$$\Psi_{\frac{3}{2}} = \frac{\phi \left\{ \alpha_{\frac{3}{2}} \tilde{\lambda}_{\frac{3}{2}} \left[\eta_{\frac{3}{2}} \left(L_{\frac{3}{2}} + D \right) + \eta_{\frac{1}{2}} B \right] + \alpha_{\frac{1}{2}} \tilde{\lambda}_{\frac{1}{2}} \left[\eta_{\frac{3}{2}} C - \eta_{\frac{1}{2}} \left(L_{\frac{1}{2}} + D \right) \right] \right\}}{L_{\frac{3}{2}} - L_{\frac{1}{2}}} \quad (22)$$

and,

$$\Psi_{\frac{1}{2}} = \frac{\phi \left\{ \alpha_{\frac{3}{2}} \tilde{\lambda}_{\frac{3}{2}} \left[-\eta_{\frac{3}{2}} \left(L_{\frac{1}{2}} + D \right) - \eta_{\frac{1}{2}} B \right] + \alpha_{\frac{1}{2}} \tilde{\lambda}_{\frac{1}{2}} \left[-\eta_{\frac{3}{2}} C + \eta_{\frac{1}{2}} \left(L_{\frac{3}{2}} + D \right) \right] \right\}}{L_{\frac{3}{2}} - L_{\frac{1}{2}}}. \quad (23)$$

The total yield of fusion particles from a single muon can be obtained by integrating Eq. (19) over times $[0, \infty)$ to obtain:

$$Y_k = - \left(\frac{\Psi_{\frac{3}{2}}}{L_{\frac{3}{2}}} + \frac{\Psi_{\frac{1}{2}}}{L_{\frac{1}{2}}} \right). \quad (24)$$

The above representation of the kinetics is the exact solution to the two-node approximation used in Zmeskal *et al.* [13], and verifies the solution presented therein to within 1% accuracy.

- [1] W. H. Breunlich, P. Kammel, J. S. Cohen, and M. Leon, *Ann. Rev. Nucl. Part. Sci.* **39**, 311 (1989).
- [2] L. I. Ponomarev, *Contemp. Phys.* **31**, 219 (1990).
- [3] P. Froelich, *Adv. Phys.* **41**, 405 (1992).
- [4] J. S. Cohen, in *Review of Fundamental Processes and Application of Atoms and Ions*, edited by C.D. Lin, World Scientific, Singapore (1993).
- [5] P. E. Knowles *et al.*, *Nucl. Instrum. Methods A* **368**, 604 (1996).
- [6] G. M. Marshall *et al.*, in *Muonic Atoms and Molecules*, edited by L. A. Schaller and C. Petitjean (Birkhäuser Verlag, CH-4010 Basel, 1993), pp. 251–260, [Proceedings of the Int. Workshop on Muonic Atoms and Molecules, Ascona].
- [7] P. Kammel, in *Muonic Atoms and Molecules*, edited by L. A. Schaller and C. Petitjean (Birkhäuser Verlag, CH-4010, Basel, 1993), pp. 111–128, [Proceedings of the Centro Stefano Franscini, Ascona].

- [8] P. E. Knowles *et al.*, Hyp. Int. **101/102**, 21 (1996).
- [9] P. E. Knowles, Ph.D. thesis, University of Victoria, 1996, unpublished.
- [10] P. Strasser, Ph.D. thesis, University of Tokyo, 1994, unpublished.
- [11] D. L. Demin *et al.*, Hyp. Int. **101/102**, 13 (1996).
- [12] A. Scrinzi *et al.*, Phys. Rev. A **47**, 4691 (1993).
- [13] J. Zmeskal *et al.*, Phys. Rev. A **42**, 1165 (1990).
- [14] J. S. Cohen, Phys. Rev. A **27**, 167 (1983).
- [15] G. Y. Korenman and S. I. Rogovaya, Yad. Fiz. **22**, 754 (1975), [Sov. J. Nucl. Phys., **22**, 389–393 (1976)].
- [16] M. Leon and H. A. Bethe, Phys. Rev. **127**, 636 (1962).
- [17] W. Czaplinski *et al.*, Phys. Rev. A **50**, 518 (1994).
- [18] E. C. Aschenauer *et al.*, Phys. Rev. A **51**, 1965 (1995).
- [19] V. E. Markushin, Phys. Rev. A **50**, 1137 (1994).
- [20] J. B. Kraiman *et al.*, Phys. Rev. Lett. **63**, 1942 (1989).
- [21] D. J. Abbott *et al.*, Phys. Rev. A **55**, 214 (1997).
- [22] E. A. Vesman, Pis'ma Zh. Eksp. Teor. Fiz. **5**, 113 (1967), [JETP Lett., **5**, 91–93 (1967)].
- [23] L. I. Man'shikov *et al.*, Zh. Eksp. Teor. Fiz. **92**, 1173 (1987), [Sov. Phys. JETP, **65**(4), 656–663 (1987)].
- [24] M. P. Faïfman, L. I. Menshikov, and T. A. Strizh, Muon Catal. Fusion **4**, 1 (1989).
- [25] M. P. Faïfman, Muon Catal. Fusion **4**, 341 (1989).
- [26] A. Scrinzi, Muon Catal. Fusion **5/6**, 179 (1990/91).
- [27] M. P. Faïfman *et al.*, Hyp. Int. **101/102**, 179 (1996).
- [28] A. Adamczak, Hyp. Int. **101/102**, 113 (1996).
- [29] L. Bracci *et al.*, Muon Catal. Fusion **5/6**, 21 (1990/91).
- [30] L. Bracci *et al.*, Muon Catal. Fusion **4**, 247 (1989).
- [31] P. E. Knowles *et al.*, Hyp. Int. **82**, 521 (1993).
- [32] P. C. Souers, *Hydrogen Properties for Fusion Energy* (University of California Press, Berkeley, California, 1986).
- [33] M. C. Fujiwara *et al.*, Hyp. Int. **101/102**, 641 (1996).
- [34] M. Lifshitz and P. Singer, Phys. Rev. C **22**, 2135 (1980).
- [35] F. Hartmann *et al.*, Technical Report No. R-94-04, PSI, (unpublished), PSI Annual Report 1995/Annex I.
- [36] C. Petitjean *et al.*, Hyp. Int. **101/102**, 1 (1996).
- [37] L. I. Men'shikov and V.V. Filchenkov, Hyp. Int. **101/102**, 207 (1996).
- [38] G. M. Hale, Muon Catal. Fusion **5/6**, 227 (1990/91).
- [39] D. V. Balin *et al.*, Pis'ma Zh. Eksp. Teor. Fiz. **40**, 318 (1984), [JETP Lett., **40**, 1112–1114 (1984)].
- [40] D. V. Balin *et al.*, Phys. Lett. B **141**, 173 (1984).
- [41] C. Petitjean *et al.*, Muon Catal. Fusion **2**, 37 (1988).
- [42] D. V. Balin *et al.*, Muon Catal. Fusion **5/6**, 163 (1990/91).
- [43] N. Nägele *et al.*, Nucl. Phys. A **493**, 397 (1989).
- [44] V. P. Dzhelepov *et al.*, Zh. Eksp. Teor. Fiz. **101**, 1105 (1992), [Sov. Phys. JETP, **74**(4), 589–595 (1992)].
- [45] A. Adamczak, Muon Catal. Fusion **4**, 31 (1989).
- [46] P. Kammel *et al.*, Phys. Lett. B **112**, 319 (1982).

TABLE I. Summary of the data.

Hydrogen [mg·cm ⁻² · (foil) ⁻¹]	Name	μ^- ($\times 10^6$)	% stopped in hydrogen
10.54(53) D ₂	Thick Deuterium	216.611	53(3)%
2.11(11) D ₂	Thin Deuterium	163.908	14(2)%
0	Bare Target	18.504	na
1.06(6) ¹ H ₂	Thin Protium	48.974	14(2)%

5.27(27) $^1\text{H}_2$	Thick Protium	59.797	53(3)%
-------------------------	---------------	--------	--------

TABLE II. Standard values used for the fits.

Parameter	Value	Source
ω_s	0.122(3)	Experiment: Balin <i>et al.</i> [40]
ϕ	1.4269(4)	Experiment: R.H. Sherman in [41]
$\tilde{\lambda}_{\frac{1}{2}\frac{3}{2}}$	$0 \mu\text{s}^{-1}$	Detailed balance of $\tilde{\lambda}_{\frac{3}{2}\frac{1}{2}}$ at 3 K
$\lambda_{\frac{1}{2}}$	$0.044(5) \mu\text{s}^{-1}$	Review: Scrinzi <i>et al.</i> [12]
P_s	0.560	Theory: Faïfman, [25]
β_s	0.47	Theory: Hale, [38]
β_p	0.580(5)	Experiment: Balin <i>et al.</i> [39]

TABLE III. The kinetics values resulting from fits to the individual detector spectra.

Parameter	neutron		proton	
	thick D ₂	thick D ₂	thick D ₂	thin D ₂
$\lambda_{\frac{3}{2}\frac{1}{2}} [\mu\text{s}^{-1}]$	35.3(1.4)	34.7(1.5)	38.6(3.1)	
$\lambda_{\frac{3}{2}} [\mu\text{s}^{-1}]$	3.12(14)	2.77(12)	2.97(23)	
$\phi_z \lambda_z [\mu\text{s}^{-1}]$	0.288(15)	0.340(12)	0.589(24)	
ϵ_a	0.14(4) %	na	na	
σ [ns]	1.48(11)	9.52(28)	9.02(36)	
χ^2/dof	158/150	164/157	162/157	
cl	55%	33%	39%	

TABLE IV. The kinetics values resulting from a simultaneous fit to both neutron and proton spectra from the thick deuterium target, see the text for a complete explanation. The fixed values are taken from Table II.

Parameter	Value(Statistical)(Systematic)			
$\lambda_{\frac{3}{2}\frac{1}{2}} [\mu\text{s}^{-1}]$		34.2(8)(1)		34.0(8)(1)
$\lambda_{\frac{3}{2}} [\mu\text{s}^{-1}]$		2.71(7)(32)		3.21(51)(16)
$\phi_z \lambda_z [\mu\text{s}^{-1}]$		0.320(10)(1)		0.320(10)(1)
$\tilde{\lambda}_{\frac{1}{2}} [\mu\text{s}^{-1}]$	fixed	fixed	fixed	0.052(8)(3)
P_s	0.47(8)(6)	fixed	fixed	fixed
β_s	fixed	0.487(15)(11)	fixed	fixed
β_p	fixed	fixed	0.563(14)(11)	fixed

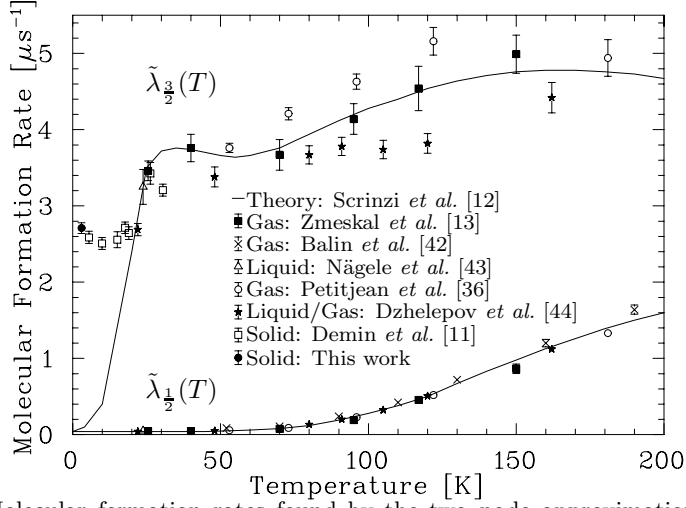


FIG. 1. Molecular formation rates found by the two-node approximation fit to data measured in solid, liquid and gas, and calculations of rates in liquid and gas. Statistical uncertainties are given, and the $\lambda_{\frac{3}{2}}$ values of Demin *et al.* [11] have been normalized to $\tilde{\lambda}_{\frac{1}{2}} = 0.044$ over their 5–30 K temperature range.

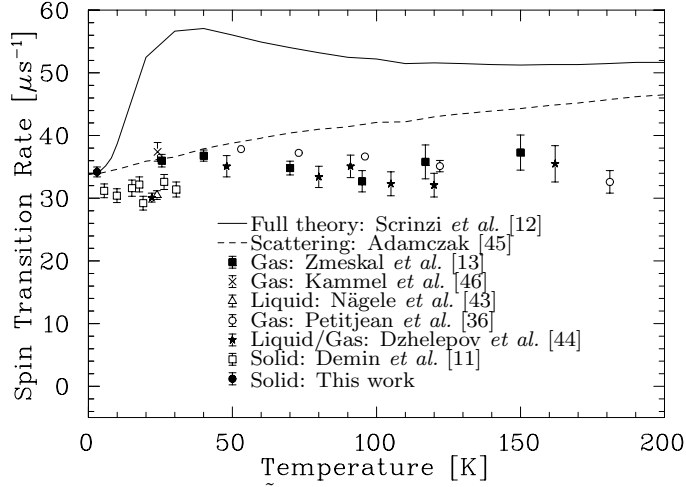


FIG. 2. Hyperfine transition rate $\tilde{\lambda}_{\frac{3}{2}, \frac{1}{2}}$. Theory calculations are shown for scattering only (dashed line) and for scattering plus back decay (solid line).

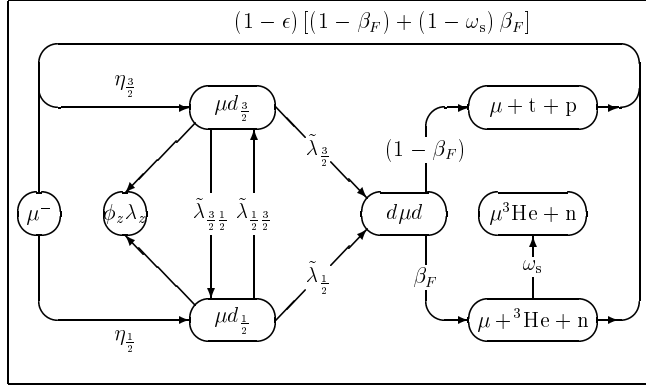


FIG. 3. The two-node approximation of the deuterium fusion kinetics. See the Appendix for details and definitions.

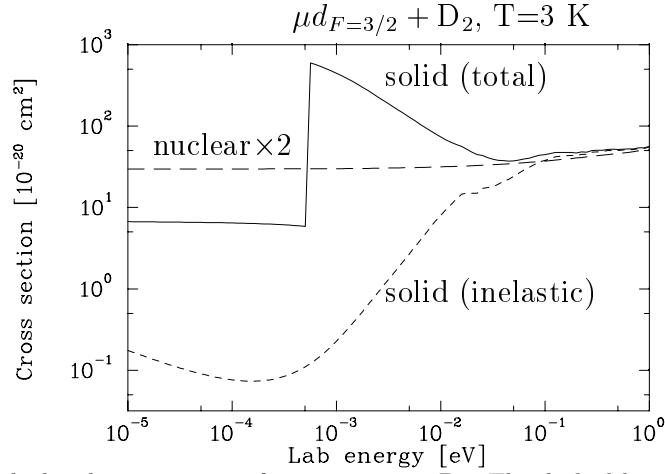


FIG. 4. Calculated cross sections for scattering in D_2 . The dashed line shows the first order approximation to the cross section on free molecules. Note the logarithmic scale, the suppression of the inelastic scattering, and the Bragg cutoff for elastic scattering. See [28] for a description of the calculations.

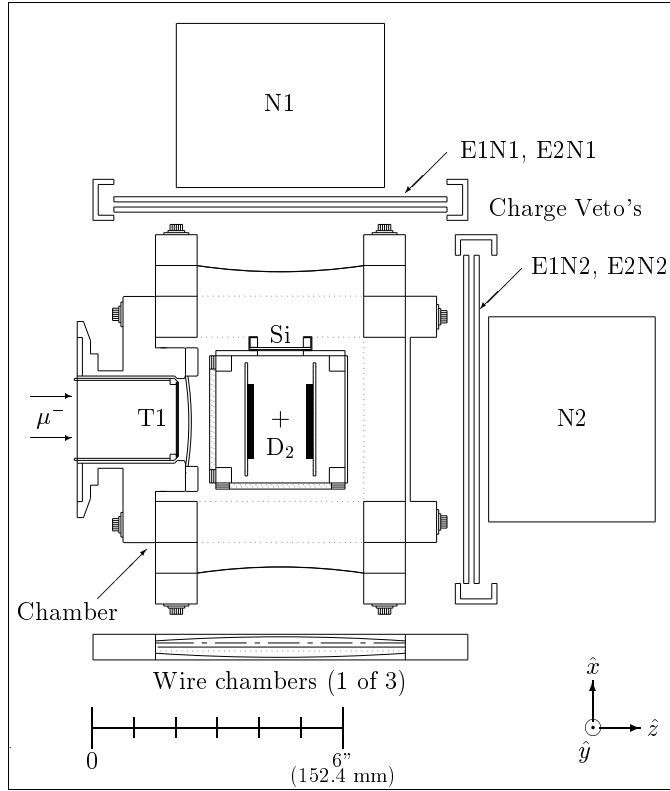


FIG. 5. A top view of the detector positions with respect to the target. Not shown are the remaining two wire chambers, scintillators, and Sodium Iodide crystal which constituted the imaging system, nor the Germanium detector, which, when in use, replaced neutron detector N1.

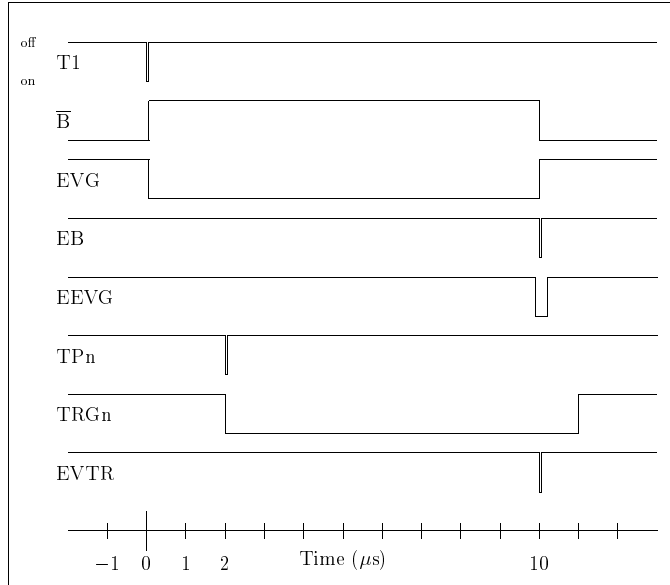


FIG. 6. The timing diagram for the trigger electronics. Time is indicated horizontally, and NIM logic level *on/off*, indicated by the lower/higher lines. The relationship between the various signals is explained in the text.

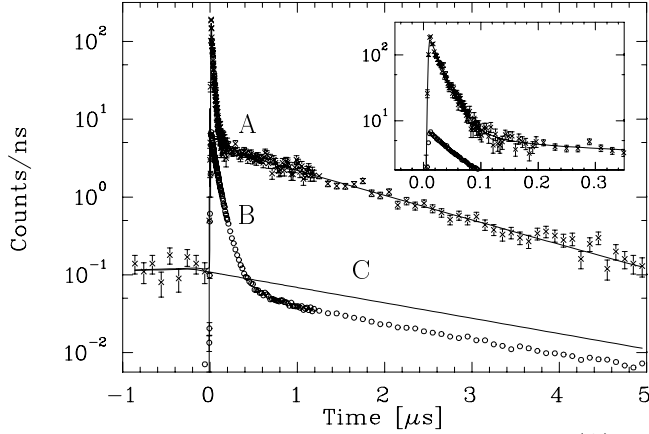


FIG. 7. Neutron time data associated with Eq. 7. Data points (A) are the del_e spectrum. Points (B)(circle) show the ϵ_a -scaled contribution of the raw spectrum. Curve (C)(line) is the representation of the other backgrounds, fit assuming a constant value before time zero, and a muon lifetime after time zero. The fitted contribution of the fusion neutrons (n_f) is shown as the solid line passing among points (A).

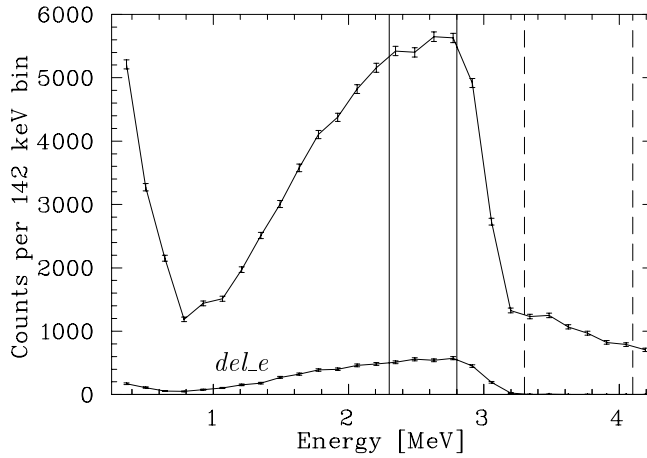


FIG. 8. A plot of the silicon energy spectrum for solid deuterium. The 3 MeV proton peak is spread due to energy loss in the thick target. Note the strong suppression of the background in the del_e spectrum. The vertical lines show the h (dashed) and l (solid) energy cut regions.

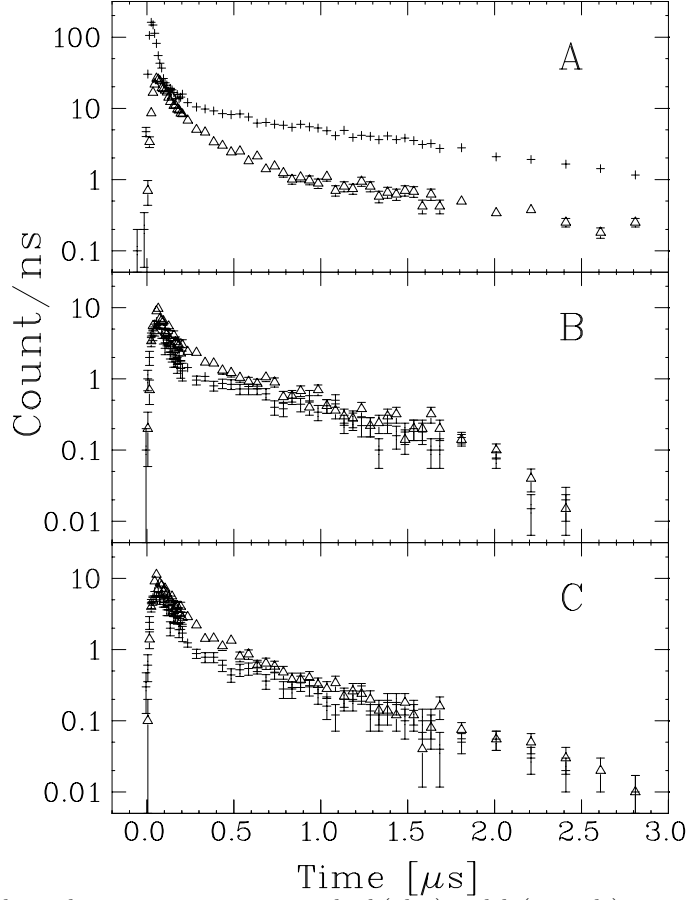


FIG. 9. Silicon detector time spectra in the *l* (plus) and *h* (triangle) regions in A) thick solid deuterium, B) bare target, and C) thick protium target. For B) and C) the *l* spectrum is systematically lower than the *h* spectrum during early times.

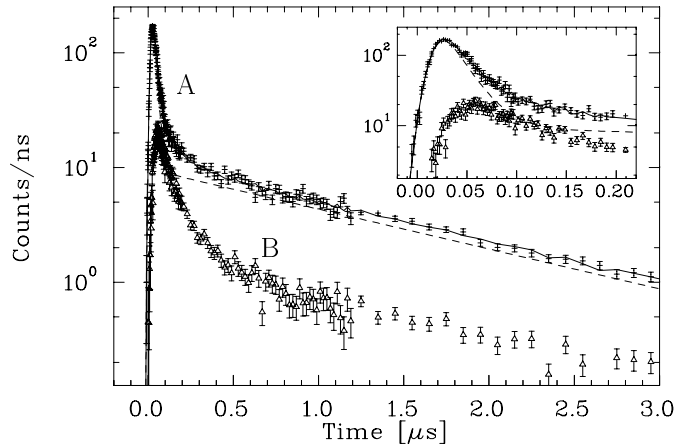


FIG. 10. Curve (A)(plus) are the proton fusion data measured in the *l* energy region. Curve (B)(triangle) shows the background as determined from the *h* energy region and the scaling function $f(t)$. The solid line is the fit and the dashed line shows the contribution of the fusion kinetics.

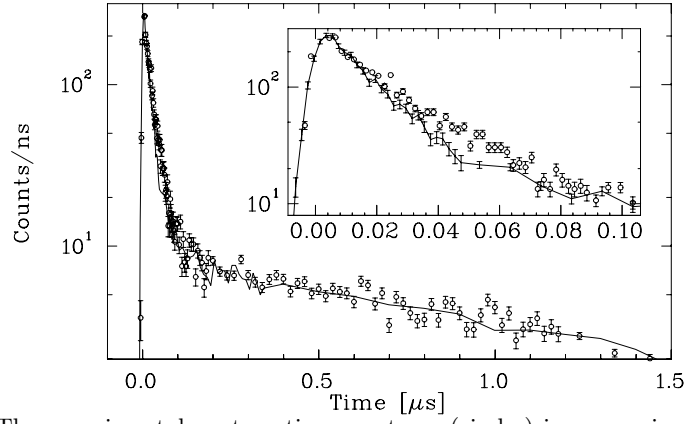


FIG. 11. The experimental neutron time spectrum (circles) in comparison with Monte Carlo predicted spectrum (line) scaled by a single normalizing factor. The inset shows also the uncertainty in the MC spectrum, illustrating the discrepancy at early times.